Pore-level Ostwald ripening of CO_2 foams at reservoir pressure

Benyamine Benali[1] · Aleksandra Sæle[1] · Na Liu[1] · Martin A. Fernø[1] ·
Zachary Paul Alcorn[1]

Abstract

The success of foam to reduce CO_2 mobility in CO_2 enhanced oil recovery and CO_2 storage operations depends on foam stability in the reservoir. Foams are thermodynamically unstable, and factors such as surfactant adsorption, the presence of oil, and harsh reservoir conditions can cause the foam to destabilize. Pore-level foam coarsening and anti-coarsening mechanisms are not, however, fully understood and characterized at reservoir pressure. Using lab-on-a-chip technology, we probe dense (liquid) phase CO_2 foam stability and the impact of Ostwald ripening at 100 bars using dynamic pore-scale observations. Three types of pore-level coarsening were observed: (1) large bubbles growing at the expense of small bubbles, at high aqueous phase saturations, unrestricted by the grains; (2) large bubbles growing at the expense of small bubbles, at low aqueous phase saturation, restricted by the grains; and (3) equilibration of plateau borders. Type 3 coarsening led to stable CO_2 foam states eight times faster than type 2 and ten times faster than type 1. Anti-coarsening where CO_2 diffused from a large bubble to a small bubble was also observed. The experimental results also compared stabilities of CO_2 foam generated with hybrid nanoparticle–surfactant solution to CO_2 foam stabilized by only surfactant or nanoparticles. Doubling the surfactant concentration from 2500 to 5000 ppm and adding 1500 ppm of nanoparticles to the 2500 ppm surfactant-based solution resulted in stronger foam, which resisted Ostwald ripening. Dynamic pore-scale observations of dense phase CO_2 foam revealed gas diffusion from small, high-curvature bubbles to large, low-curvature bubbles and that the overall curvature of the bubbles decreased with time. Overall, this study provides in situ quantification of CO_2 foam strength and stability dynamics at high-pressure conditions.

Article Highlights

- A comprehensive laboratory investigation of CO_2 foam stability and the impact of Ostwald ripening.
- Pore-level foam coarsening and anti-coarsening mechanisms insights.

Extended author information available on the last page of the article

🌲 Springer

1 Introduction

Carbon capture, utilization, and sequestration (CCUS) is essential for limiting global warming and achieving the climate goals of the Paris Agreement (IPCC, Climate Change 2014). CCUS involves capturing CO_2 from industrial sources, such as cement plants or power plants, and injecting it into subsurface reservoirs for enhanced oil recovery (EOR) and geological carbon sequestration (Metz et al. 2005). CO_2 injection for EOR and carbon storage has been widely implemented over the last decades (Eiken et al. 2011; Taber et al. 1997). Although CO_2 EOR and sequestration have been successfully performed, the effectiveness of CO_2 EOR and CO_2 storage is limited by challenges associated with high CO_2 mobility and reservoir heterogeneity (Hanssen et al. 1994). The low viscosity and density of CO_2 compared to other reservoir fluids can lead to viscous fingering and gravity override, while reservoir heterogeneity can cause channeling through high-permeability zones (Talebian et al. 2014; Mo et al. 2012; Alcorn et al. 2020a). This results in poor volumetric sweep efficiency, high producing gas–oil ratios, low oil recovery, and reduced CO_2 sequestration capacity (Lake et al. 2014). CO_2 foam can reduce these flow instabilities by increasing CO_2 viscosity, reducing its relative permeability, and diverting flow from high- to lower-permeability zones (Rossen 1996; Sæle et al. 2022; Enick et al. 2012; Føyen et al. 2020).

Foam is a dispersion of a discontinuous gas phase (CO_2) in a continuous liquid phase (David and Marsden 1969). Foam can be generated in the porous media by injecting a foaming solution such as surfactant and/or nanoparticles and CO_2, either simultaneously or in alternating slugs (Shan and Rossen 2004). To maintain the stability of surfactant-based foams in the reservoir is challenging due to various factors such as surfactant adsorption, the presence of oil, and at harsh reservoir conditions, which can cause the foam to break (Sheng and Sheng 2013). Nanoparticles can add stability to surfactant-based foams by withstanding high-temperature and high-salinity conditions (Eide et al. 2018). However, nanoparticles alone generate weak foam compared to surfactants (Alcorn et al. 2020b; Soyke et al. 2021). Recent research has shown that the addition of silica nanoparticles to surfactant-based foam may increase the stability and improve displacement efficiency for CO_2 EOR and CO_2 storage applications (Chaturvedi and Sharma 2021; Singh and Mohanty 2016). Nanoparticles can become trapped in the plateau border and lamellae, which hinder coalescence and liquid drainage (Singh and Mohanty 2014).

CO_2 foam bubbles are separated by continuous liquid films called lamellae, and the location of where three lamellae meet is referred to as a plateau border. Foams are thermodynamically unstable, and their longevity depends on the stability of single lamellae (Farajzadeh et al. 2012). After bubble generation, lamellae move and rearrange to achieve minimum interfacial free energy (Aronson et al. 1994). This results in a change in foam texture (size and the number of bubbles), which is driven by three mechanisms: (1) drainage, where lamella thinning is caused by gravity or capillary suction (Kovscek and Radke 1993; Yu and Kanj 2022), (2) coalescence, where bubbles unite and form larger bubbles due to lamella rupture (Langevin 2019), and (3) coarsening, where gas diffuses through lamella due to capillary pressure differences, known as Ostwald ripening (Benali et al. 2022).

Foam coarsening during a CO_2 foam flood for EOR is unfavorable as it leads to an increase in CO_2 foam mobility, resulting in a reduction in sweep efficiency. The stability of bulk foams is typically measured by the decrease in the volume or height of the foam with time, and these instabilities are mainly related to drainage and coalescence mechanisms (Yu and Kanj 2022; Yekeen et al. 2017). In porous media, the bubbles are the similar size

or larger than the pore bodies (Osei-Bonsu et al. 2017). When CO_2 is injected, a high fraction (> 0.97) of bubbles become trapped due to large capillary forces (Benali et al. 2022). At pore scale, the drainage mechanism is insignificant due to the more dominant effect of surface forces compared to the volumetric forces (Yu and Kanj 2022). Bubble coalescence is also significantly reduced and can be neglected for surfactant-based foams where the surfactants improve the interfacial properties of the lamella and constrain bubble rupture (Yu et al. 2022; Huang et al. 2017). Therefore, Ostwald ripening is the critical mechanism affecting foam stability in porous media.

Ostwald ripening is a well-known phenomenon in bulk systems (Greenwood 1956; Lifshitz and Slyozov 1961; Voorhees 1985, 1992). It occurs due to the transport of gas from smaller bubbles with small radius, high curvature, and high internal pressure to larger bubbles with large radius, low curvature, and low internal pressure resulting in the disappearance of smaller bubbles (Saint-Jalmes 2006; Marchalot et al. 2008). However, the process is more complex in porous media, because the bubbles cannot freely grow, and the coarsening is affected by the geometric confinement of the pores (Yu and Kanj 2022; Xu et al. 2019). Ostwald ripening in porous media typically leads to stable states, due to both bubble coarsening and anti-coarsening. The anti-coarsening phenomenon occurs when bubbles are deformed by the geometric confinement of the pore network leading to a reversed gas diffusion from larger bubbles to smaller bubbles (Huang et al. 2017; Xu et al. 2017). An analytical investigation estimated the timescale required for a disconnected gas phase to reach equilibrium in a gas and brine configuration within porous media and found that at the field scale, the timescale to reach equilibrium is estimated to be millions of years, whereas at the laboratory scale the timeframe ranged from a few weeks to a year (Blunt 2022).

Pore-scale experiments show that the coarsening does not conform to the unrestricted growth laws (Wang et al. 2021). Instead, the bubbles coarsen to the pore size, and at the end of the coarsening, the lamellae rest in minimum-energy configurations in the pore throats (Xu et al. 2017; Jones et al. 2018). The grains, pore network, and pore throat sizes affect the Ostwald ripening mechanism and can result in different bubble shapes and sizes, i.e., foam texture (Huang et al. 2017; Mehmani and Xu 2022). In previous studies, reaching local equilibrium differs based on the pore size of the media. For media comprised of submicron pores, local equilibrium can be achieved within 1 s. However, for media comprised of 1-mm pores, it may take decades to achieve local equilibrium (Yu et al. 2023). Therefore, performing experiments in a realistic pore network is crucial to understanding CO_2 foam dynamics in porous media.

Micromodels can be used for direct visualization of CO_2 foam flow through porous media. They are two-dimensional flow cells that contain a pore network and transparent glass for visualization (Gogoi and Gogoi 2019). High-pressure micromodels are ideal for studying CO_2 foam at reservoir conditions and enable gathering quantitative and qualitative data of the Ostwald ripening mechanism by using image analysis techniques to monitor the bubble size and distribution (Gizzatov et al. 2021; Rognmo et al. 2019). Additionally, high-resolution three-dimensional X-ray imaging can examine pore-scale phenomena in core plugs. This imaging technique was utilized to investigate various phenomena, including the Ostwald ripening of hydrogen within the pore space of a Bentheimer core plug (Zhang et al. 2023; Gao et al. 2023).

Few attempts have been made to understand dense phase CO_2 foam coarsening and anti-coarsening mechanisms in a realistic pore network at reservoir pressure. However, it is critical to gain an in-depth understanding of pore-scale CO_2 foam phenomena because interfacial tension, viscosity, and density are different at high-pressure conditions. CO_2 density and viscosity increase at higher pressures, whereas the interfacial tension decreases

at higher pressures. Therefore, the aim of this work was to study the Ostwald ripening mechanism for a static dense phase CO_2 foam generated with different foaming solutions in a realistic pore network at 100 bars and 23 °C. A secondary objective was to compare CO_2 foam generated by hybrid nanoparticle–surfactant solution to CO_2 foam stabilized by only surfactant or nanoparticles. The foam bubbles were monitored using high-resolution images acquired by a Zeiss microscope. Quantitative data were obtained by image analysis using Python libraries as OpenCV and skimage.

2 Materials and methods

2.1 Fluid preparation

Brine (3.5 wt% NaCl) with fluorescein sodium salt (500 PPM $C_{20}H_{10}Na_2O_5$, F6377 Sigma-Aldrich) was used for all aqueous phases (Table 1), where the fluorescent tracer was added to the solution to distinguish between the water and CO_2 phases. All the aqueous solutions were filtered using a sterile 0.2-µm cellulose acetate filter (514-0061, VWR) before being injected into the micromodel. Two foaming agents were used: (1) Surfonic L24-22, a non-ionic, water-soluble surfactant with linear ethoxylated alcohol from Indorama Ventures, and (2) Levasil CC301, a surface-modified spherical silica nanoparticle from Nouryon. CO_2 of 99.999% purity was used for foam generation and to saturate the aqueous solution before injecting it into the micromodel. Four foaming solutions were prepared by mixing brine with surfactant, nanoparticle, or a hybrid combination of both (Table 1).

2.2 Micromodel and holder

The high-pressure micromodel enabled direct visualization of pore-scale interactions between different fluids and rock grains at reservoir conditions (Gogoi and Gogoi 2019). It consisted of an optically transparent borosilicate glass on the top bonded to an etched silicon wafer with a representative pore structure. The 2D pore network was generated from thin sections of a natural sandstone and etched on the silicon wafer by the deep reactive ion etching method with a constant depth of 30 µm to get vertical pore walls and sharp edges. However, when reproducing a 3D porous matrix obtained from a real reservoir rock to 2D, some modifications were made to connect all the pores, resulting

Table 1 Composition of aqueous solutions and cleaning solutions

| Aqueous solution	Concentration, Component
Brine	35 000 ppm, NaCl
Fluorescent dye	500 ppm, fluorescein sodium salt
Surfactant (SF) 5000	5000 ppm, Surfonic L24-22
Surfactant (SF) 2500	2500 ppm, Surfonic L24-22
Surfactant (SF) 2500 + Nanoparticle (NP) 1500	2500 ppm, Surfonic L24-22 + 1500 ppm, Levasil CC301
Nanoparticle (NP) 1500	1500 ppm, Levasil CC301
IPA	877 000 ppm, 2-propanol–water azeotrope
Hydrogen peroxide	300 000 ppm, H_2O_2
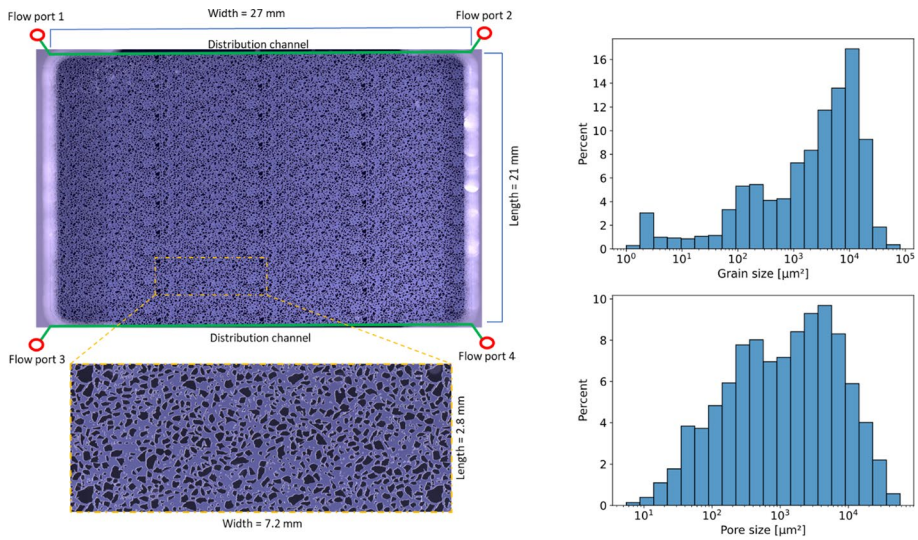
Fig. 1 Left: Dimensions of the entire micromodel and the unique pore network with the locations of the fluid flow ports and distribution channels. Right: Characteristic features of the micromodel from one of the 36 repetitions of the pattern where the top graph shows grain sizes and the bottom graph shows pore size distribution. The average grain and pore sizes are 6238 μm^2 and 3896 μm^2, respectively

Table 2 Pore network properties

Parameter	Value
Width	27 mm
Length (without channels)	21 mm
Depth	30 μm
Porosity	0.61
Permeability	2.97 Darcy
Average pore size	3896 μm^2
Unique pore network repetition	36
Pattern size	7.2 mm×2.8 mm
Tortuosity (x-axis)	1.881
Tortuosity (y-axis)	1.998
Wettability	Water-wet

in higher porosity and permeability compared to cylindrical sandstone samples (Buchgraber et al. 2012). The unique pore network (7.2×2.8 mm) was repeated 36 times (4×9) with an overlap, resulting in a total pore network of 27×21 mm (Fig. 1). In addition, the micromodel had two etched fluid distribution channels (200 μm width), one at the top and one at bottom. Four flow ports were etched through the silicon wafer to connect with external environments. Micromodel properties are summarized in Table 2. The porosity and permeability were calculated to be 0.61 and 2.97 Darcy, respectively (Benali 2019). The pore volume (PV) with a constant etching depth of 30 μm was 11.1 μL (Benali 2019). The pores were classified using snow algorithm (Gostick et al. 2019), and the average pore size was 3896 μm^2.

The micromodel holder was designed and manufactured in-house from PEEK and aluminum materials. The first part made of PEEK had four threaded holes in the bottom side that aligned with the micromodel flow ports. The micromodel was placed on the top of the O-rings on the first part, and the second part made of aluminum was attached. The second part had an open window for direct visualization of the micromodel. Detailed steps for mounting the micromodel in holder with images can be found in Haugen et al. (2023).

2.3 Experimental setup and procedures

Images of the pore network were acquired using a microscope (Axio Zoom. V16, Zeiss) equipped with both brightfield and fluorescence channels. The brightfield channel used a cold-light source and a diffuser S for uniform illumination, whereas the fluorescence channel used a 38 HE Green fluorescent reflector to track the phase with the fluorescent tracer. A motorized scanning stage enabled high-resolution image acquisition by using 121 tiles (11×11). Two images were captured for each tile and then stitched together within a time frame of 4 min and 37 s to obtain images of the whole pore network at two channels (fluorescence channel image and brightfield channel image) (Fig. 3).

Figure 2 shows a schematic of the experimental setup for visualization of CO_2 foam. The setup was designed to enable high-pressure experiments. A back pressure regulator (BPR) was placed at the end of experimental setup connecting with a N_2 cylinder at 100 bars. The select valves used in this setup allow injection and production from all the flow ports, but in this study port 1 was used for CO_2 injection and port 4 was used for production. The switch valve was used to inject incompressible fluids directly into the micromodel using the pump with distilled water as driving force. The cleaning solutions were
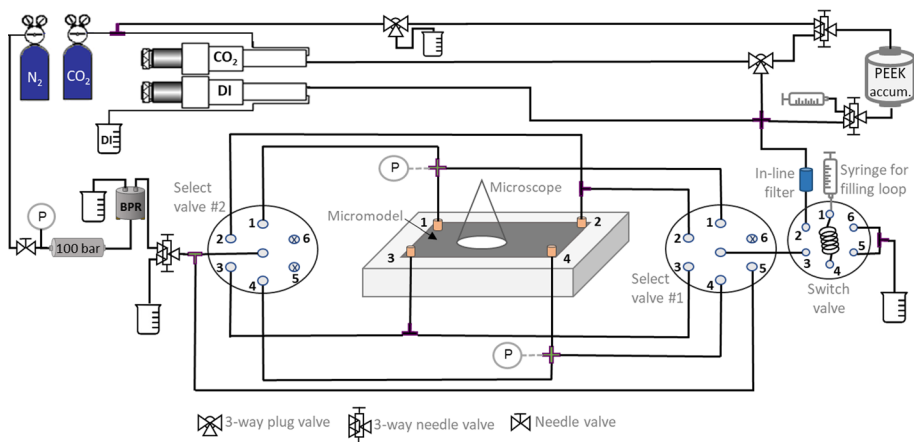

Fig. 2 Schematic of the experimental setup used for pore-scale foam studies in the micromodel. The micromodel was assembled in the holder positioned underneath the microscope. The lines were connected to the ports from the bottom side of the holder but are shown at the top in the figure for illustration. A high-precision plunger pump (Quizix Q5000-2.5K) was used for fluid injection. The DI cylinder was used for injection of the distilled water or driving the fluids in the loop in the switch valve, whereas CO_2 cylinder was used for CO_2 injection or driving the fluids from the PEEK accumulator. Two six-port select valves (Idex, MXP7970-000) were used, one at the inlet (#1) and one at the outlet (#2), to ensure constant dead volume. In addition, a two-position switch valve (Idex, 9725) was used to facilitate variable fluid injection without need for additional pumps

injected into the 1-mL filling loop in the switch valve using a syringe, then the switch valve passed through the loop, and the solutions were pressurized the same as the system (Fig. 2). Prior to injection into the pore network, all aqueous solutions were saturated with liquid CO_2 at experimental conditions, enabling the intensity of fluorescence dye to stay constant when contacting CO_2. Before each experiment, the pore network was cleaned with distilled water, 2-propanol–water azeotrope (IPA), and hydrogen peroxide (H_2O_2). H_2O_2 was used to maintain the same surface conditions before each experiment. The CO_2 was in the liquid phase at experimental conditions of 100 bars and 23 °C (Lemmon et al. 2023).

Two repetitions of five static CO_2 foam experiments were performed (four with foaming solutions listed in Table 1 and one with only brine for comparison). Investigation of Ostwald ripening mechanism for a static CO_2 foam in porous media at high pressure requires stable CO_2 saturation in the field of view (FoV). The experiments were designed so that the CO_2 saturation was constant throughout the experiment. To achieve this, the following procedure was used:

1. Pre-saturate the micromodel with the CO_2-saturated solution at a constant volumetric flow rate (2 μL/min) using port 1 for injection and port 4 for production.
2. Inject CO_2 at a constant volumetric flow rate (2 μL/min) for 2 h, to generate foam with high CO_2 saturation and bubble number, using port 1 for injection and port 4 for production.
3. Inject the aqueous solution at a constant volumetric flow rate (1 μL/min) to remove the CO_2 bubbles in the distribution channels and isolate foam in the pore network, from port 1 to port 2, and port 3 to port 4 for 1 h each (5.4 PV each).
4. Hold constant pressure in the micromodel, with the distilled water pump, using port 1 for injection while the production line was closed. $T = 0$ in results and discussion section refers to this step, when the distilled water pump is connected to the micromodel.

Despite isolation of the foam, dissolution of CO_2 bubbles into the aqueous phase was observed in the top left side of the micromodel. The dissolution was caused by CO_2 diffusion into the distilled water within the pump through the inlet (port 1). The aqueous phase in the micromodel and inlet lines was pre-saturated with CO_2, but the CO_2 diffused to the distilled water pump used to hold the pressure. Therefore, the dissolved area was removed from the analyzed FoV for each experiment.

2.4 Image processing and analysis

Image segmentation was conducted to obtain quantitative data for each CO_2 bubble throughout the experiments. Image thresholding is the most challenging task during image processing. It transfers a grayscale image with a range of pixel values into a binary image of two-pixel values, which consist of a background and a foreground. In this work, the CO_2 bubble properties needed to be analyzed. Therefore, the background consisted of the grains and aqueous phase and the foreground consisted of CO_2 bubbles. Cropped images acquired with fluorescence and brightfield channels, and their corresponding grayscale histograms are shown in Fig. 3.

The fluorescence and brightfield images were transformed into grayscale to calculate the corresponding grayscale histograms. Then, the histograms were used to separate the image into two or three classes using the Multi-Otsu algorithm from scikit-image library (Walt et al. 2014). The Multi-Otsu algorithm was used to calculate appropriate

thresholding values. The fluorescence channel image was separated into two classes, where each class was in the foreground at this stage. The first class contained grains and CO_2 signals, whereas the second class contained the water phase (fluorescent tracer) (Fig. 3a, c). The brightfield channel image was separated into three classes (Fig. 3d) following two steps. In the first step, the histogram with pixel values from 0 to 50 were used to calculate
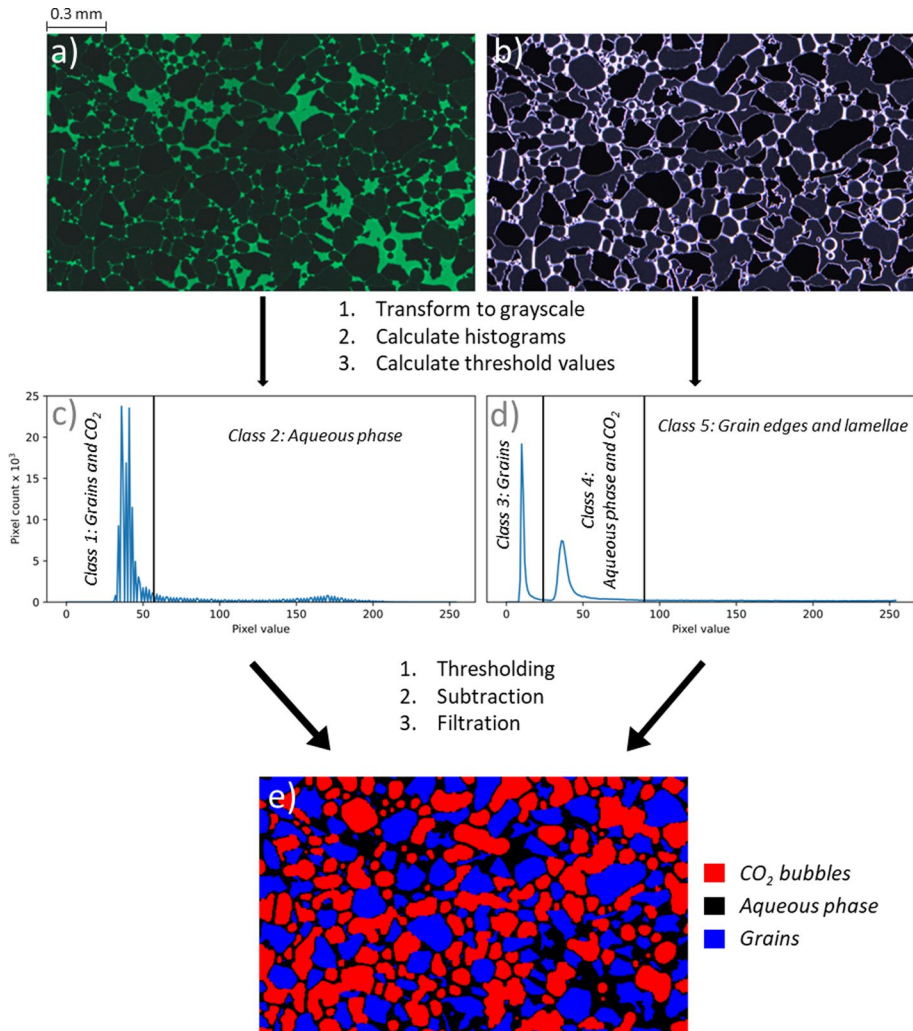

Fig. 3 Illustration of the segmentation process. **a** Fluorescence channel image (2.2 mm × 1.3 mm) of the micromodel with CO_2 foam and aqueous phase occupying the pores, CO_2, and grains appear black, whereas aqueous phase with fluorescent tracer appears green. **b** Brightfield channel image from same size, position, and time as **a** grains appear black, aqueous phase and CO_2 appear purple, and grain edges and lamella appear white. **c** and **d** Grayscale image histogram plots corresponding to the images above. The black vertical lines shown in the histogram plots are the thresholding values calculated using the multi-Otsu algorithm (Walt et al. 2014). The possible classes to obtain from each channel are shown in the histograms. **e** Illustration of results, blue areas represent the grains, red areas are discrete CO_2 bubbles, and black areas are the continuous water phase

the first threshold value, and the grains were classified as foreground in the first class. In the second step, the histogram was used from the first threshold value to the end of the histogram (pixel value 255) to calculate the second threshold value. The aqueous phase and CO_2 were classified as a foreground in the second class, whereas the grain edges and lamellae were classified as a foreground in the third class (Fig. 3b, d). Subtraction of class 3 (grains) and class 5 (grain edges and lamellae) from class 1 (grains and CO_2) results in a binary image of separated bubbles and some noise. The morphology function from OpenCV (Bradski 2000) was used with 1×3 and 3×1 kernels to remove noise. Figure 3e illustrates the grains, CO_2 bubbles, and the aqueous phase in different colors. The CO_2 saturation is underestimated due to subtraction of thick lamellae and filtration.

Ostwald ripening occurs due to the diffusion of gas from smaller high-curvature bubbles to larger low-curvature bubbles. Therefore, the bubble shape was described quantitatively using a roundness equation:

$$\text{Roundness} = \frac{4\pi \times \text{Area}}{\text{Perimeter}^2}$$

The roundness equals one for a circular shape and goes down to zero for highly non-circular shapes.

3 Results and discussion

3.1 CO₂ saturation

To separate Ostwald ripening from other effects, it was important that the dense CO_2 phase saturation was constant as a function of time (see Fig. 4). After an initial increase, the CO_2 saturation for CO_2 foam generated with surfactant-based solutions was constant within experimental uncertainty in the FoV. For CO_2 foam stabilized with nanoparticles, the CO_2 saturation decreased with time because the nanoparticle-based foam consisted of very large CO_2 bubbles that were more exposed to the water phase and gradually dissolved. The CO_2 saturation without foaming agent was constant during the first 30 h and then decreased because of CO_2 dissolution.

The finely textured surfactant-based foams trapped more CO_2 and showed higher CO_2 saturation (on average 0.50) relative to nanoparticle (0.36) and brine (0.29) that did not generate stable foam and lower CO_2 trapping. Silica nanoparticles are known for stabilizing, rather than generating, foam, and brine did not generate foam due to the lack of a foaming agent (Alcorn et al. 2020b). The hybrid nanoparticle–surfactant solution trapped more CO_2 (0.53) compared with pure surfactant-based foam (on average 0.49), and doubling the surfactant concentration (from 2500 to 5000 ppm) increased the CO_2 trapping by two percent PV due to the generation of finer textured foam which may be beneficial for CO_2 storage applications. Previous studies have reported increased oil recovery and CO_2 storage capacity using hybrid nanoparticle–surfactant solution (Chaturvedi and Sharma 2021; Worthen et al. 2014; AlYousef et al. 2017).

3.2 Bubble roundness

Ostwald ripening leads to bubble coarsening due to the diffusion of gas from smaller, high-curvature bubbles to larger, low-curvature bubbles (see Fig. 5). Pore-level images showed
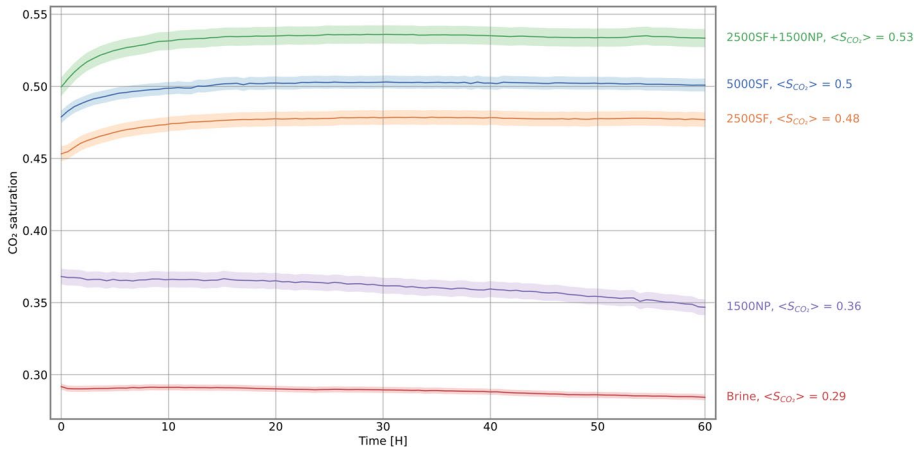
Fig. 4 The average CO_2 saturation as a function of time for repeated experiments conducted with foaming solutions and brine, and their corresponding standard deviation (shaded area). The CO_2 saturation for CO_2 foam generated with surfactant-based solutions (green, blue, and orange lines) was constant from 10 h and throughout the experiments. The increase at the start was due to diffusion of very small bubbles that could not be tracked by image analysis into larger bubbles. The highest CO_2 saturation (53% of pore volume) was achieved using hybrid nanoparticle–surfactant solution (2500SF + 1500NP). The average CO_2 saturation without counting for the first 10 h for the experiments conducted with surfactant was 0.50, 0.48, 0.53, 0.36, and 0.29 for 5000SF, 2500SF, 2500SF + 1500NP, 1500NP, and brine, respectively. The CO_2 saturation for 1500NP decreased with time because nanoparticle-based foam consisted of very large CO_2 bubbles that were more exposed to the aqueous phase and hence dissolved a little
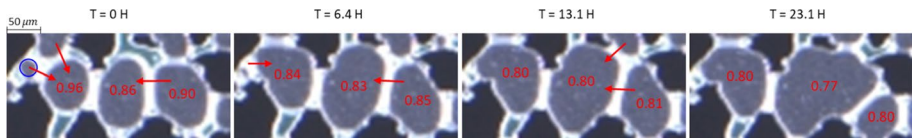

Fig. 5 Sequential composed images showing static CO_2 foam. Red arrow shows the direction of CO_2 diffusion. The bubble roundness is indicated by red values inside corresponding bubbles. The images are from 5000SF at the same FoV (0.33 mm × 0.16 mm)

a small bubble (blue circle, initial size 449 μm^2, Fig. 5) being consumed by a larger bubble (initial size 3644 μm^2), with a resulting accumulation of the aqueous phase in the original location of the small bubble. During this process, the roundness of the larger bubbles decreased with time (from on average 0.91 to on average 0.79); hence, coarsening occurred. As coarsening ensued, the aqueous phase on top of lamellae was pushed to the top side of the image resulting in less bubble roundness.

Pore-level foam stability depends on several factors, including bubble roundness, bubble size, and the position of lamellae. Typically, high-curvature bubbles have higher energy and are less stable than low-curvature bubbles. The average bubble roundness (Fig. 6) was higher using 2500SF foaming solution compared to solutions with higher foaming agent concentration (2500SF + 1500NP, 5000SF), indicating less stable foam at lower concentrations. Previous studies have reported generation of stronger and more stable CO_2 foams at higher surfactant concentrations (Phukan et al. 2020). The average bubble roundness for surfactant-based foams decreased over time, and the rate of change was comparable for all
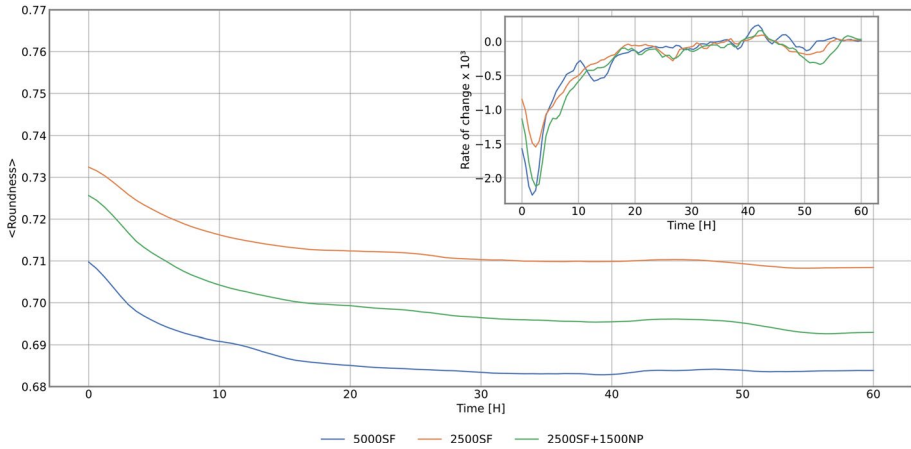
Fig. 6 The average roundness for repeated experiments conducted with surfactant and nanoparticles-based solutions (5000SF, 2500SF, and 2500SF + 1500NP). The inset plot shows the rates of change in the average bubble roundness. Bubbles generated with 2500SF solution had the most roundness, the next was bubbles generated with 2500SF + 1500NP solution, and bubbles generated with 5000SF solution had the least roundness. The overall trend of average roundness is equal for the three solutions. The rate of change reached zero after around 2 h for all three solutions and reached equilibrium after 30 h

foaming agents, indicating the influence of pore geometry on the evolution of roundness. The rate of change in bubble roundness for the three solutions decreased at the start, reaching a minimum after 2 h, and then increased toward zero. The rate of change reached zero after around 30 h for all three solutions. However, after 40 h the rate of change for the average roundness increased (Fig. 6, inset plot) and resulted in a further decrease in the average roundness because of coarsening. The average roundness approached equilibrium again between 55 and 60 h. The experiments conducted with only brine or nanoparticles (1500 NP) were not plotted because the bubbles were stable, and their roundness did not change with time. The average roundness of bubbles generated with brine and 1500 NP was 0.70 and 0.56, respectively.

3.3 Coarsening and anti-coarsening of CO$_2$ foam

Three types of coarsening were observed in this study: (1) large spherical bubbles in open pore network growing at the expense of small bubbles at high aqueous phase saturations (Fig. 7); (2) large bubbles growing at the expense of small bubbles, at low aqueous phase
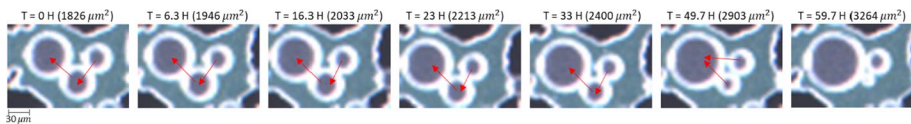

Fig. 7 Sequential composed images showing an example of type 1 coarsening of static CO$_2$ foam. The size of the largest bubble is tracked, and to find next to the time of images. Red arrows show the direction of CO$_2$ diffusion. The largest bubble with low curvature grows at the expense of smaller bubbles with high-curvature, unrestricted by the porous media in a high aqueous phase saturation. The images are from 5000SF at the same FoV (0.18 mm×0.12 mm)

saturation, restricted by the grains (Fig. 8); and (3) equilibration of plateau borders at low aqueous phase saturation (Fig. 9).

Type 1 coarsening resembles bulk systems, where the largest spherical bubbles with low-curvature grow at the expense of smaller bubbles with high curvature based on Young–Laplace defined pressure difference, unrestricted by the porous media (Fig. 7). The presence of foaming agents reduced coarsening, and equilibrium was not achieved even after 60 h, indicated by the gradual increase in the bubble area (Fig. 7). Type 2 coarsening showed that CO_2 bubbles were constricted by the grains, and the aqueous saturation was low compared to type 1 coarsening (Fig. 8). Type 2 coarsening was driven by lamella movement toward minimum-energy configuration at the pore throats. The number of bubbles decreased, whereas the largest bubbles (initially 41,701 μm^2) grew (Fig. 8). Overall, type 2 coarsening led to the disappearance of small bubbles with high curvature, due to diffusion of CO_2 from smaller bubbles to the larger bubbles, resulting in a system with lower average bubble curvature.

Sequentially composed images of the pore network revealed that most lamellae were in the pore throats at the minimum-energy configuration. However, some lamellae were also found in the middle of the pores if the bubbles were positioned with an equilibrium curvature in relation to each other (Yu et al. 2022). Type 3 coarsening occurred when lamellae were in a minimum-energy state positioned in the middle of the pores (Fig. 9). A plateau border is where three lamellae are connected. The lamellae are at minimum-energy configuration when the angles for all the interfaces between the bubbles in the plateau border
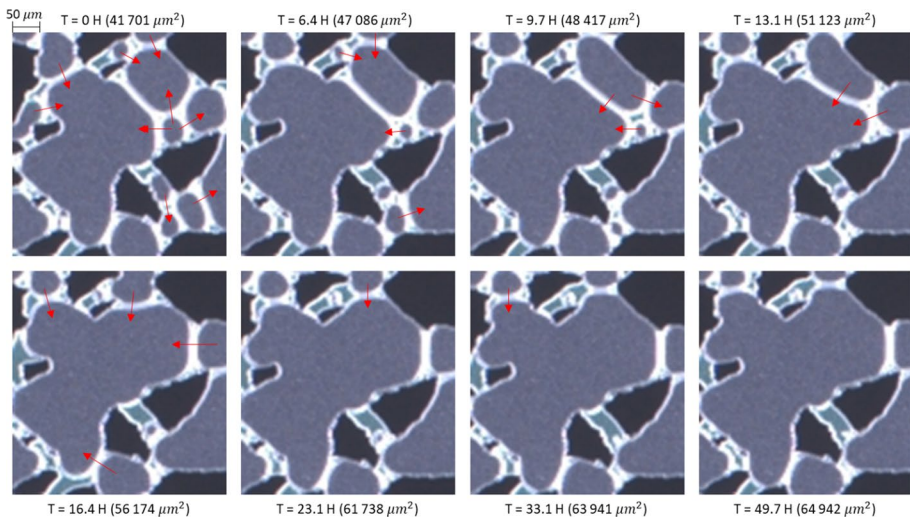

Fig. 8 Sequential composed images showing example of type 2 coarsening of static CO_2 foam. The size of the largest bubble is tracked, and to find next to the time of images. Red arrows show the direction of CO_2 diffusion. From 0 to 13.1 h, the number of arrows decreased from 9 to 2, small bubbles disappeared, and large bubbles grew. The largest bubble moved toward the top right corner in the time interval from 13.1 to 16.4 h, and this made the water flow from the left bottom to top left, and some lamellae were moved from the minimum-energy configuration. This destabilization of lamellae led to further coarsening, and the number of arrows increased to 4. Type 1 coarsening led to the disappearance of small bubbles with high curvature, and diffusion of CO_2 from those bubbles to the larger bubbles resulting in a system with lower curvature. Due to the wettability of the micromodel, water accumulation in narrow pores was observed. The images are from 5000SF at the same FoV (0.39 mm×0.41 mm)
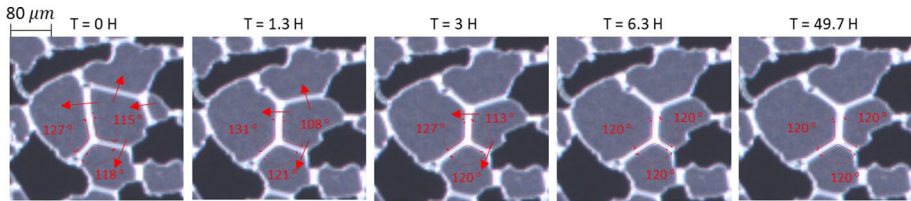
Fig. 9 Sequential composed images showing example of type 3 coarsening of static CO_2 foam. Red arrows show the direction of CO_2 diffusion. Plateau border is where three lamellae are connected; the angles are drawn on the plateau border in the bottom of the images. The angles at the start are not 120 degrees, and that causes the plateau border to reposition, and the CO_2 starts to diffuse between the bubbles. This repositioning of the plateau border caused creation of a new plateau border and the disappearance of the small bubble in the right of the image because the lamella was pushed toward the pore throat. Type 3 coarsening leads to equilibrium while the lamellae are still in the middle of the pores. The lamellae can be at minimum-energy configuration when the angles for all the interfaces between the bubbles in the plateau border equal 120 degree. The images are from 5000SF at the same FoV (0.34 mm×0.32 mm)

equal 120 degree, even if the lamellae are in the middle of the pore. At time zero in Fig. 9, the angles at the plateau border are not 120 degrees, and that causes the plateau border to reposition and triggering CO_2 diffusion between the bubbles. The plateau border reached equilibrium after 6 h when all the angles reached 120 degrees. The angles between three bubbles must be precisely 120 degrees each in order for the three forces acting on the interface to achieve equilibrium. Type 3 coarsening led to stable CO_2 foam states eight times faster than type 2 and ten times faster than type 1. In type 3 coarsening, the lamellae are freer to move, without friction with the pore walls; therefore, the foam reaches equilibrium faster than type 2 coarsening which had friction from the pore walls. For type 1 coarsening, the aqueous saturation was high, and the CO_2 diffusion was slower due to the thick lamellae and the larger distance between the bubbles.

Several studies have reported that diffusion direction can reverse so that CO_2 is transported from large bubbles to small bubbles, a phenomenon called anti-coarsening (Yu et al. 2022; Huang et al. 2017; Xu et al. 2017). We also observed anti-coarsening here (Fig. 10). When the system was close to equilibrium (most lamellae at minimum-energy configuration at pore throats), a lamella moved toward the pore throat due to the capillary suction. This was because the micromodel was water-wet and the lamella was drawn toward the pore throat, causing diffusion of CO_2 from the larger bubble (initially 17,585 μm^2) to the smaller bubble (initially 8357 μm^2).

The average bubble area with surfactant-based solutions increased with time due to the Ostwald ripening effect (see Fig. 11). The normalized average area increased rapidly in the time interval from 0 to 10 h compared to the time interval from 10 to 60 h with a decreasing rate of change (Fig. 11, inset plot). The rapid increase at the start was because all coarsening types are trying to reach equilibrium, hence coarsening the CO_2 foam rapidly. After 10 h, type 3 coarsening was already at equilibrium and the rate of change for type 2 decreased, whereas type 1 coarsening was a very slow process, and almost linear in the experimental time. Anti-coarsening mechanism did not affect the normalized average area because it does not remove bubbles (only repositions lamellae) and the average area remains constant. Bubbles generated with 2500SF solution reached the largest bubble size and had the highest average bubble roundness, indicating that the foam was weaker and less stable, compared to bubbles generated with 2500SF + 1500 NP solution and bubbles generated with 5000SF solution. Doubling the surfactant concentration from 2500 to

5000 ppm resulted in stronger foam indicated by lower normalized average area, which resisted Ostwald ripening. Adding 1500 ppm of nanoparticles to the 2500 ppm surfactant-based solution resulted in stronger foam. However, the rate of destabilization during the time interval from 0 to 10 h was higher with nanoparticles. This can be attributed to the increased concentration of nanoparticles on the CO_2 interface as the bubbles shrink. Interfacial tension measurements of melt poly and supercritical CO_2 reveal that increasing the nanoparticle concentration from 0 to 2 wt% leads to a decrease in interfacial tension. For nanoparticle concentrations higher than 2 wt%, the interfacial tension continues to decrease (Sarikhani et al. 2015). Experiments conducted with only brine or nanoparticles (1500 NP) were not included in the analysis because their normalized average area did not change
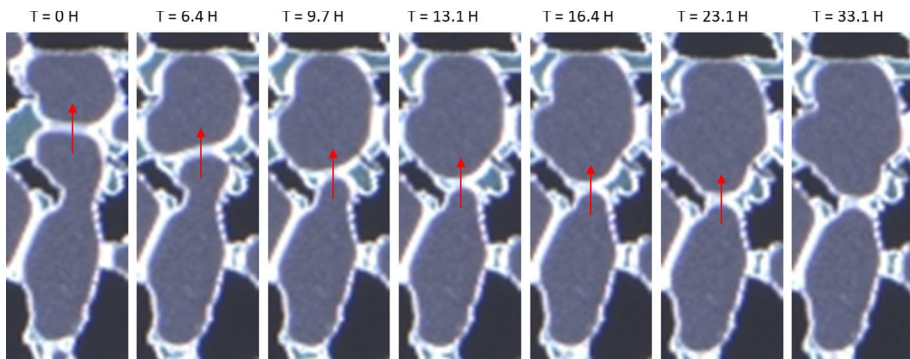

Fig. 10 Sequential composed images showing anti-coarsening of static CO_2 foam. CO_2 is transported from the larger bubble to the smaller bubble, and lamella moves from the middle of the top pore to the pore throat in the middle. The images are from 5000SF at the same FoV (0.17 mm×0.43 mm)
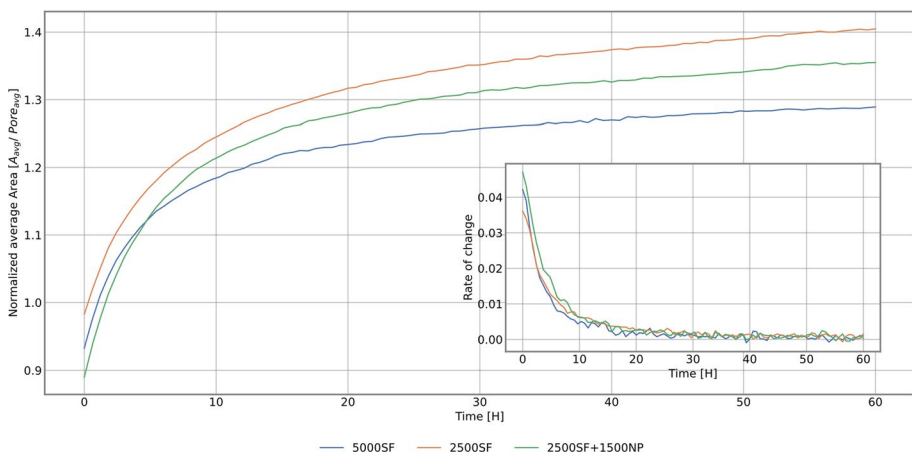

Fig. 11 The normalized average area for repeated experiments conducted with surfactant and nanoparticles-based solutions (5000SF, 2500SF, and 2500SF+1500NP). The rates of change in the normalized average area are plotted as inset plot. Bubbles generated with 2500SF solution reached the highest bubble size, followed by bubbles generated with 2500SF+1500 NP solution, and bubbles generated with 5000SF solution
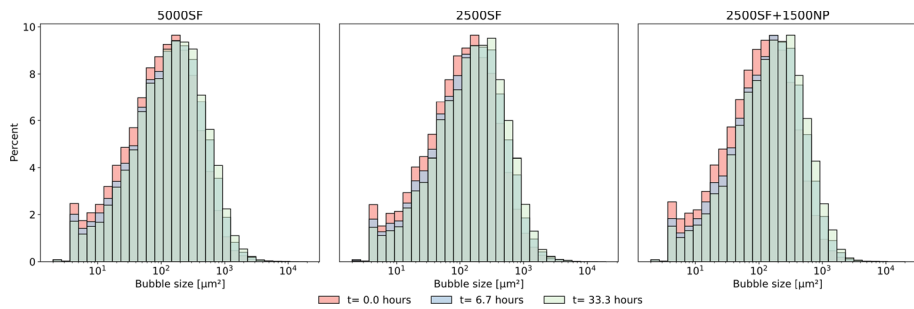
Fig. 12 The bubble size distribution of repeated experiments conducted with surfactant-based solutions (5000SF, 2500SF, and 2500SF+1500NP) at three different time steps (0, 6.6, and 33.3 h). The bubble size distribution progressively shifted toward the right side of the plots, indicating coarsening of the bubbles

with time. The average normalized average bubble area with brine and 1500 NP was 17.2 and 3.2, respectively.

The bubble size distribution was compared for three time steps using histograms in the presence of surfactant-based solutions, as illustrated in Fig. 12. The bubble size distribution progressively shifted toward the right side of the plot, aligning more closely with the pore size distribution. The histograms revealed a reduction in the number of small bubbles (less than 100 μm^2), as indicated by reduction of the bubble percentage on the left side of the histogram maxima, resulting in the disappearance of smaller bubbles over time. Conversely, the number of larger bubbles (greater than 100 μm^2), represented by the right side of the histogram maxima, increased, indicating the coalescence of bubbles in the presence of the surfactant-based solution.

4 Conclusion

This work studied the Ostwald ripening mechanism for static CO_2 foams generated with different foaming solutions in a realistic pore structure at 100 bars. Ostwald ripening was the dominant mechanism of foam destabilization. Sequentially composed images of the pore network revealed gas diffusion from small, high-curvature bubbles to large, low-curvature bubbles, and the overall curvature of the bubbles decreased with time. We have observed three types of coarsening. The first coarsening type was characterized by large bubbles growing at the expense of small bubbles, at high aqueous phase saturations, unrestricted by the grains. The second coarsening type was characterized by large bubbles growing at the expense of small bubbles, at low aqueous phase saturation, restricted by the grains. The third coarsening type was characterized by equilibration of plateau borders. We observed anti-coarsening phenomena, where CO_2 diffused from a large bubble to a small bubble. The experimental results also compared CO_2 foam generated by hybrid nanoparticle–surfactant foaming solution to CO_2 foam stabilized by only surfactant or nanoparticles. The foam generated with surfactant-based solutions achieved the highest CO_2 saturation compared to solutions with only nanoparticles or brine. Doubling the surfactant concentration from 2500 to 5000 ppm and adding 1500 ppm of nanoparticles to the 2500 ppm surfactant-based solution resulted in stronger foam, which resisted Ostwald ripening. Overall, this study provides in situ quantification of CO_2 foam strength and stability dynamics at high-pressure conditions.

Data availability The raw foam injection micromodel images and Python scripts are available from the corresponding author on reasonable request.

Declarations

Conflict of interest The authors declare that they have no known competing financial interests or personal relationships that could have appeared to influence the work reported in this paper.

References

Alcorn, Z.P., Fredriksen, S.B., Sharma, M., Føyen, T., Wergeland, C., Fernø, M.A., Graue, A., Ersland, G.: Core-scale sensitivity study of CO_2 foam injection strategies for mobility control, enhanced oil recovery, and CO_2 storage. E3S Web Conf. **146**, 02002 (2020a)

Alcorn, Z.P., Føyen, T., Gauteplass, J., Benali, B., Soyke, A., Fernø, M.: Pore- and core-scale insights of nanoparticle-stabilized foam for CO_2-enhanced oil recovery. Nanomaterials **10**(10), 1917 (2020b)

AlYousef, Z., Almobarky, M., Schechter, D.: Surfactant and a mixture of surfactant and nanoparticles stabilized-CO_2/Brine foam for gas mobility control and enhance oil recovery. In: Carbon Management Technology Conference (2017)

Aronson, A.S., Bergeron, V., Fagan, M.E., Radke, C.J.: The influence of disjoining pressure on foam stability and flow in porous media. Colloids Surf. A **83**(2), 109–120 (1994)

Benali, B.: Quantitative Pore-Scale Analysis of CO_2 Foam for CCUS. The University of Bergen, Bergen (2019)

Benali, B., Føyen, T.L., Alcorn, Z.P., Haugen, M., Gauteplass, J., Kovscek, A.R., Fernø, M.A.: Pore-scale bubble population dynamics of CO_2-foam at reservoir pressure. Int. J. Greenh. Gas Control **114**, 103607 (2022)

Blunt, M.J.: Ostwald ripening and gravitational equilibrium: implications for long-term subsurface gas storage. Phys. Rev. E **106**(4), 045103 (2022)

Bradski, G.: The openCV library. Dr. Dobb's J. Softw. Tools Prof. Program. **25**(11), 120–123 (2000)

Buchgraber, M., Al-Dossary, M., Ross, C.M., Kovscek, A.R.: Creation of a dual-porosity micromodel for pore-level visualization of multiphase flow. J. Pet. Sci. Eng. **86–87**, 27–38 (2012)

Chaturvedi, K.R., Sharma, T.: In-situ formulation of pickering CO_2 foam for enhanced oil recovery and improved carbon storage in sandstone formation. Chem. Eng. Sci. **235**, 116484 (2021)

David, A., Marsden, S.S.: The rheology of foam. In: Fall Meeting of the Society of Petroleum Engineers of AIME. OnePetro (1969)

Eide, Ø., Føyen, T., Skjelsvik, E., Rognmo, A., Fernø, M.: Nanoparticle stabilized foam in harsh conditions for CO_2 EOR. In: Abu Dhabi International Petroleum Exhibition & Conference (2018)

Eiken, O., Ringrose, P., Hermanrud, C., Nazarian, B., Torp, T.A., Høier, L.: Lessons learned from 14 years of CCS operations: Sleipnern, in Salah and Snøhvit. Energy Procedia **4**, 5541–5548 (2011)

Enick, R.M., Olsen, D., Ammer, J., Schuller, W.: Mobility and conformance control for CO2 EOR via thickeners, foams, and gels-a literature review of 40 years of research and pilot tests. In: SPE Improved Oil Recovery Symposium. OnePetro (2012)

Farajzadeh, R., Andrianov, A., Krastev, R., Hirasaki, G.J., Rossen, W.R.: Foam–oil interaction in porous media: implications for foam assisted enhanced oil recovery. Adv. Coll. Interface Sci. **183–184**, 1–13 (2012)

Føyen, T., Brattekås, B., Fernø, M., Barrabino, A., Holt, T.: Increased CO_2 storage capacity using CO_2-foam. Int. J. Greenh. Gas Control **96**, 103016 (2020)

Gao, Y., Sorop, T., Brussee, N., van der Linde, H., Coorn, A., Appel, M., Berg, S.: Advanced digital-SCAL measurements of gas trapped in sandstone. Petrophys. SPWLA J. Form. Eval. Reserv. Descr. **64**(03), 368–383 (2023)

Gizzatov, A., Pierobon, S., AlYousef, Z., Jian, G., Fan, X., Abedini, A., Abdel-Fattah, A.I.: High-temperature high-pressure microfluidic system for rapid screening of supercritical CO2 foaming agents. Sci. Rep. **11**(1), 3360 (2021)

Gogoi, S., Gogoi, S.B.: Review on microfluidic studies for EOR application. J. Pet. Explor. Prod. Technol. **9**(3), 2263–2277 (2019)

Gostick, J.T., Khan, Z.A., Tranter, T.G., Kok, M.D., Agnaou, M., Sadeghi, M., Jervis, R.: PoreSpy: a python toolkit for quantitative analysis of porous media images. J. Open Source Softw. **4**(37), 1296 (2019)

Greenwood, G.: The growth of dispersed precipitates in solutions. Acta Metall. **4**(3), 243–248 (1956)

Hanssen, J.E., Holt, T., Surguchev, L.M.: Foam processes: an assessment of their potential in north sea reservoirs based on a critical evaluation of current field experience. In: SPE/DOE Improved Oil Recovery Symposium (1994)

Haugen, M., Benali, B., Føyen, T., Song, W., Fernø, M.A., Brattekås, B.: Calcite-functionalized micro-models for pore-scale investigations of CO2 storage security. E3S Web Conf. **366**, 01004 (2023)

Huang, Z., Su, M., Yang, Q., Li, Z., Chen, S., Li, Y., Zhou, X., Li, F., Song, Y.: A general patterning approach by manipulating the evolution of two-dimensional liquid foams. Nat. Commun. **8**(1), 14110 (2017)

IPCC Climate Change 2014: Synthesis Report. Contribution of Working Groups I, II and III to the Fifth Assessment Report of the Intergovernmental Panel on Climate Change [Core Writing Team, R.K. Pachauri and L.A. Meyer (eds.)]. IPCC, Geneva, Switzerland, p. 151 (2014)

Jones, S.A., Getrouw, N., Vincent-Bonnieu, S.: Foam flow in a model porous medium: I. The effect of foam coarsening. Soft Matter **14**(18), 3490–3496 (2018)

Kovscek, A.R., Radke, C.J.: Fundamentals of Foam Transport in Porous Media. Lawrence Berkeley Lab, CA (1993)

Lake, L., Johns, R.T., Rossen, W.R., Pope, G.A.: Fundamentals of Enhanced Oil Recovery. Society of Petroleum Engineers, London (2014)

Langevin, D.: Coalescence in foams and emulsions: similarities and differences. Curr. Opin. Colloid Interface Sci. **44**, 23–31 (2019)

Eric W.L., Ian H.B., Marcia L.H., and Mark O.M.: Thermophysical properties of fluid systems. In: Linstrom P.J., Mallard, W.G. (eds.) NIST Chemistry WebBook, NIST Standard Reference Database Number 69. National Institute of Standards and Technology, Gaithersburg MD (2023). https://doi.org/10.18434/T4D303

Lifshitz, I.M., Slyozov, V.V.: The kinetics of precipitation from supersaturated solid solutions. J. Phys. Chem. Solids **19**(1–2), 35–50 (1961)

Marchalot, J., Lambert, J., Cantat, I., Tabeling, P., Jullien, M.-C.: 2D foam coarsening in a microfluidic system. EPL (europhysics Letters) **83**(6), 64006 (2008)

Mehmani, Y., Xu, K.: Pore-network modeling of Ostwald ripening in porous media: How do trapped bubbles equilibrate? J. Comput. Phys. **457**, 111041 (2022)

Metz, B., Davidson, O., De Coninck, H., Loos, M., Meyer, L.: IPCC Special Report on Carbon Dioxide Capture and Storage. Cambridge University Press, Cambridge (2005)

Mo, D., Yu, J., Liu, N., Lee, R.: Study of the Effect of Different Factors on Nanoparticle-Stablized CO2 Foam for Mobility Control. In: SPE Annual Technical Conference and Exhibition (2012).

Osei-Bonsu, K., Grassia, P., Shokri, N.: Relationship between bulk foam stability, surfactant formulation and oil displacement efficiency in porous media. Fuel **203**, 403–410 (2017)

Phukan, R., Gogoi, S.B., Tiwari, P.: Effects of CO2-foam stability, interfacial tension and surfactant adsorption on oil recovery by alkaline-surfactant-alternated-gas/CO_2 flooding. Colloids Surf. A **597**, 124799 (2020)

Rognmo, A.U., Fredriksen, S.B., Alcorn, Z.P., Sharma, M., Føyen, T., Eide, Ø., Graue, A., Fernø, M.: Pore-to-core EOR upscaling for CO_2 foam for CCUS. SPE J. **24**(06), 2793–2803 (2019)

Rossen, W.: Foams in enhanced oil recovery. In: Prud'homme, R.K., Khan, S.A. (eds.) Foams—Theory, Measurement, and Applications, pp. 413–464. Marcel Dekker Inc, New York (1996)

Sæle, A., Graue, A., Alcorn, Z.: Unsteady-state CO_2 foam injection for increasing enhanced oil recovery and carbon storage potential. Adv. Geo-Energy Res. **6**, 472–481 (2022)

Saint-Jalmes, A.: Physical chemistry in foam drainage and coarsening. Soft Matter **2**(10), 836–849 (2006)

Sarikhani, K., Jeddi, K., Thompson, R.B., Park, C.B., Chen, P.: Adsorption of surface-modified silica nanoparticles to the interface of melt poly(lactic acid) and supercritical carbon dioxide. Langmuir **31**(20), 5571–5579 (2015)

Shan, D., Rossen, W.R.: Optimal injection strategies for foam IOR. SPE J. **9**(02), 132–150 (2004)

Sheng, J.J.: Chapter 11 - foams and their applications in enhancing oil recovery. In: Sheng, J.J. (ed.) Enhanced oil recovery field case studies, pp. 251–280. Gulf Professional Publishing, Boston (2013)

Singh, R. and Mohanty, K.K.: Synergistic stabilization of foams by a mixture of nanoparticles and surfactants. In: SPE Improved Oil Recovery Symposium. OnePetro (2014)

Singh, R., Mohanty, K.K.: Foams stabilized by in-situ surface-activated nanoparticles in bulk and porous media. SPE J. **21**(01), 121–130 (2016)

Soyke, A., Benali, B., Føyen, T., Alcorn, Z.P.: Hybrid nanoparticle-surfactant stabilized foams for CO_2 mobility control at elevated salinities. In: IOR 2021, vol. 2021, pp. 1–14. European Association of Geoscientists & Engineers, Dubai (2021)

Taber, J.J., Martin, F.D., Seright, R.S.: EOR screening criteria revisited—part 1: introduction to screening criteria and enhanced recovery field projects. SPE Reserv. Eng. **12**(03), 189–198 (1997)

Talebian, S.H., Masoudi, R., Tan, I.M., Zitha, P.L.J.: Foam assisted CO2-EOR: a review of concept, challenges, and future prospects. J. Pet. Sci. Eng. **120**, 202–215 (2014)

Van der Walt, S., Schönberger, J.L., Nunez-Iglesias, J., Boulogne, F., Warner, J.D., Yager, N., Gouillart, E., Yu, T.: Scikit-image: image processing in Python. PeerJ **2**, e453 (2014)

Voorhees, P.W.: The theory of Ostwald ripening. J. Stat. Phys. **38**(1), 231–252 (1985)

Voorhees, P.W.: Ostwald ripening of two-phase mixtures. Annu. Rev. Mater. Sci. **22**(1), 197–215 (1992)

Wang, C., Mehmani, Y., Xu, K.: Capillary equilibrium of bubbles in porous media. Proc. Natl. Acad. Sci. **118**(17), e2024069118 (2021)

Worthen, A.J., Parikh, P.S., Chen, Y., Bryant, S.L., Huh, C., Johnston, K.P.: Carbon dioxide-in-water foams stabilized with a mixture of nanoparticles and surfactant for CO_2 storage and utilization applications. Energy Procedia **63**, 7929–7938 (2014)

Xu, K., Bonnecaze, R., Balhoff, M.: Egalitarianism among bubbles in porous media: an ostwald ripening derived anticoarsening phenomenon. Phys. Rev. Lett. **119**(26), 264502 (2017)

Xu, K., Mehmani, Y., Shang, L., Xiong, Q.: Gravity-induced bubble ripening in porous media and its impact on capillary trapping stability. Geophys. Res. Lett. **46**(23), 13804–13813 (2019)

Yekeen, N., Idris, A.K., Manan, M.A., Samin, A.M., Risal, A.R., Kun, T.X.: Bulk and bubble-scale experimental studies of influence of nanoparticles on foam stability. Chin. J. Chem. Eng. **25**(3), 347–357 (2017)

Yu, W., Kanj, M.Y.: Review of foam stability in porous media: The effect of coarsening. J. Petrol. Sci. Eng. **208**, 109698 (2022)

Yu, W., Zhou, X., Kanj, M.Y.: Microfluidic investigation of foam coarsening dynamics in porous media at high-pressure and high-temperature conditions. Langmuir **38**(9), 2895–2905 (2022)

Yu, Y., Wang, C., Liu, J., Mao, S., Mehmani, Y., Xu, K.: Bubble coarsening kinetics in porous media. Geophys. Res. Lett. **50**(1), e2022GL100757 (2023)

Zhang, Y., Bijeljic, B., Gao, Y., Goodarzi, S., Foroughi, S., Blunt, M.J.: Pore-scale observations of hydrogen trapping and migration in porous rock: demonstrating the effect of ostwald ripening. Geophys. Res. Lett. **50**(7), e2022GL102383 (2023)

Authors and Affiliations

Benyamine Benali[1] [iD] **· Aleksandra Sæle[1] · Na Liu[1] · Martin A. Fernø[1] · Zachary Paul Alcorn[1]**

✉ Benyamine Benali
    benyamine.benali@uib.no

[1] Department of Physics and Technology, University of Bergen, Bergen, Norway